Journal of Materiomics 9 (2023) 817–823

Contents lists available at ScienceDirect

Journal of Materiomics

journal homepage: www.journals.elsevier.com/journal-of-materiomics/

High-performance photodetectors based on two-dimensional perovskite crystals with alternating interlayer cations

Yezhan Li [a], Zhengxun Lai [a], You Meng [a], Wei Wang [a], Yuxuan Zhang [a], Xuwen Zhao [a], Di Yin [a], Weijun Wang [a], Pengshan Xie [a], Quan Quan [a], SenPo Yip [b], Johnny C. Ho [a, b, c, *]

[a] Department of Materials Science and Engineering, City University of Hong Kong, 999077, Hong Kong SAR, China
[b] Institute for Materials Chemistry and Engineering, Kyushu University, Fukuoka, 816-8580, Japan
[c] State Key Laboratory of Terahertz and Millimeter Waves, City University of Hong Kong, 999077, Hong Kong SAR, China

ARTICLE INFO

Article history:
Received 22 March 2023
Received in revised form
5 May 2023
Accepted 7 May 2023
Available online 4 June 2023

Keywords:
Photodetector
Two-dimensional
Hybrid perovskite
Alternating interlayer cation
Imaging

ABSTRACT

Organic-inorganic halide perovskite, as a low-cost, solution-processable material with remarkable optoelectronic properties, is ideal candidate to fabricate high-performance photodetectors and is expected to significantly reduce device costs. Compared to the common Dion-Jacobson and Ruddlesden-Popper two-dimensional (2D) layered hybrid perovskite compounds, the perovskites with alternating cations in the interlayer (ACI) phase show higher crystal symmetry and narrower optical bandgaps, which exhibit great potential for excellent photodetection performance. Herein, we report a high-performance photodetector based on the 2D bilayered hybrid lead halide perovskite single crystal with the ACI phase ($GAMA_2Pb_2I_7$; GA = $C(NH_2)_3$ and MA = CH_3NH_3). The single-crystal photodetector exhibits high photoresponsivity of 1.56, 2.54, and 2.60 A/W for incident light wavelengths of 405, 532, and 635 nm under 9.82 nW, respectively, together with the correspondingly high detectivity values of 1.86×10^{12}, 3.04×10^{12}, and 3.11×10^{12} Jones under the same operating conditions. Meanwhile, a high-resolution imaging sensor is built based on the $GAMA_2Pb_2I_7$ single-crystal photodetector, confirming the high stability and photosensitivity of the imaging system. These results show that the 2D hybrid lead halide perovskites with alternating interlayer cations are promising for high-performance visible light photodetectors and imaging systems.

1. Introduction

Photodetectors (PDs), which can directly convert optical signals into electrical signals, play a significant part in imaging, security systems, industrial inspection, and so on [1–5]. To fabricate high-performance PDs, a semiconductor with a good ability to absorb incident photons and then produce photogenerated carriers effectively is indispensable. So far, various types of semiconductors, including silicon, group II-VI compounds, group III-V compounds, and organics, have been extensively explored for use in PDs [6–10]. However, these semiconductor materials usually require relatively complicated and expensive ways to synthesize, in which the epitaxy and vapor-liquid-solid (VLS) mechanisms are usually involved [11,12]. Thus, it is urgent to discover new promising candidates to further design the photodetector with high performance, low cost, and ease to fabricate.

Recently, the three-dimensional (3D) organic-inorganic hybrid lead halide perovskites in the forms of $CH_3NH_3PbX_3$ (X = I, Br, Cl) have received intense attention owing to their low-cost fabrication and excellent optoelectronic properties [13,14]. As a result, they have impressive developments, especially in the high-efficient perovskite solar cells [15–17]. To date, a certified photovoltaic power conversion efficiency (PCE) of hybrid perovskite solar cells has approached 25.7% (until March. 2023), which is higher than that of many reported conventional thin-film solar cells, organic photovoltaics, and dye-sensitized solar cells [18]. Moreover, this kind of material with excellent features has also attracted enormous attention in other optoelectronic devices, such as lasers, transistors, and light-emitting diodes (LEDs) [19]. Especially, perovskites have been examined for high-performance wide-spectrum photodetection from X-ray, UV, visible, to near-infrared light [20,21].

* Corresponding author. Department of Materials Science and Engineering, City University of Hong Kong, 999077, Hong Kong SAR, China.
E-mail address: johnnyho@cityu.edu.hk (J.C. Ho).
Peer review under responsibility of The Chinese Ceramic Society.

https://doi.org/10.1016/j.jmat.2023.05.003

However, the poor stability of these 3D perovskite-based devices hinders their further commercial applications [22,23].

Using short alkyl ammonium or aromatic ammonium cations to low-dimensional perovskites is an effective method to balance device stability and performance [24–26]. Based on this route, plenty of perovskites with different dimensions, including zero-dimension (0D), one-dimension (1D), and two-dimension (2D), were synthesized [27–32]. Among them, 2D perovskites show better optoelectronic performance when compared with 0D and 1D perovskites due to their layered structure being analogue to the conventional 3D perovskites [33]. From a structural perspective, 2D layered hybrid perovskites could be classified into three types: Dion-Jacobson (DJ), Ruddlesden-Popper (RP), and the newly discovered alternating cations in the interlayer (ACI) types [34–38]. The 2D ACI perovskite described by formula $(C(NH_2)_3)(CH_3NH_3)_nPb_nI_{3n+1}$, featuring two different alternating organic cations in the interlayer space, was recently presented by Kanatzidis *et al.* [36]. Compared to the more common DJ-phase and RP-phase layered hybrid perovskites, the perovskite with the ACI phase adopts the short organic cations between inorganic layers, which decrease the bandgap and exciton binding energy, being favorable for the performance improvement of optoelectronic devices [35]. For example, Yang *et al.* reported stable 2D ACI perovskite solar cells with superior PCE exceeding 19.00% [37]. In addition, a LED made of the ACI perovskites was successfully fabricated by the Hofkens's group, showing an external quantum efficiency (EQE) of 3.4% under high current density [38]. In this regard, the 2D hybrid perovskites with the ACI phase possess great potential for manufacturing high-performance photodetection with improved stability.

Herein, we synthesized 2D bilayered lead-halide hybrid perovskite single crystals with the ACI phase ($GAMA_2Pb_2I_7$; GA = $C(NH_2)_3$ and MA = CH_3NH_3) by a facile cooling crystallization method. A photodetector with a device structure of Au/$GAMA_2Pb_2I_7$/Au was successfully fabricated and displays wide-spectrum light detecting capability covering the entire visible light region. The photodetector shows high photoresponsivity of 1.56, 2.54, and 2.60 A/W, for 405, 532, and 635 nm incident light under −1.5 V bias at 9.82 nW, respectively. In addition, an imaging sensor is built based on the $GAMA_2Pb_2I_7$ single-crystal photodetector to demonstrate the high-resolution imaging capability.

2. Experimental

2.1. Material synthesis

In this work, the 2D hybrid perovskite of $GAMA_2Pb_2I_7$ crystals was synthesized using guanidine carbonate salt ($C_2H_{10}N_6{\cdot}CH_2O_3$, 99%, J&K Scientific), lead(II) acetate trihydrate ($C_4H_6O_4Pb{\cdot}_3H_2O$, 99%, Sigma-Aldrich), methylamine hydrochloride ($CH_5N{\cdot}HCl$, 99%, J&K Scientific), hypophosphorous acid (H_3PO_2, 50% (in mass) water solution, J&K Scientific) and hydroiodic acid (HI, 47%, Macklin). First, 5.4 g (59.5 mmol) guanidine carbonate salt, 4.02 g (30.0 mmol) methylamine hydrochloride, and 22.8 g (60.1 mmol) lead(II) acetate trihydrate were slowly added into a solution of 100 mL hydroiodic acid and 2 mL hypophosphorous acid. After that, a quick stir would mix them thoroughly at a temperature of 230 °C until there is no precipitation. The small $GAMA_2Pb_2I_7$ powder-like samples would appear when cooling to room temperature (20 °C/h). A yield of 76% was estimated relative to Pb. To grow the bulk perovskite crystals, a constant-speed temperature-programmable bath was used to control the cooling speed. After cooling the bath from 65 °C to room temperature (1 °C/d), millimeter-level bulk crystals were obtained (see Fig. S1). The purity of these powder and single crystal samples was confirmed by a D2 PHASER XE-T X-ray Diffractometer System. The absorption spectra were obtained using a UV-3600i Plus UV-VIS-NIR spectrometer.

2.2. Device fabrication and characterization

To fabricate the photodetection device, Au electrodes with a thickness of 50 nm were deposited by a high-vacuum thermal evaporator with an evaporation rate of about 1.8 Å/s. In a shadow masking process, the length and width of the device channel were defined to be 65 μm and 15 μm, respectively. Room temperature *I-V* and *I–T* characteristics under different incident light wavelengths (405, 532, and 635 nm) were measured using a semiconductor analyzer (Agilent 4155C). The incident light power was calibrated by PM400, Thorlabs. To obtain the high-speed response time, the precise time-resolved *I–T* curves of the $GAMA_2Pb_2I_7$ device were recorded *via* a digital oscilloscope (Tektronix, TBS 1102B) connected with a low-noise current preamplifier (Stanford Research Systems, SR570).

3. Results and discussion

As shown in the photograph in Fig. S1, black-color single crystals of $GAMA_2Pb_2I_7$ were grown from its saturated solution through the cooling crystallization method. The measured PXRD pattern agrees well with the simulation result, which confirms its crystal structure (Fig. 1c). Single-crystal structural analysis discovers that it crystallizes in the space group No. 38, orthorhombic *Bmm*2 at 293 K. Fig. 1a illustrates the 2D ACI perovskite structure, where the layered parts contain corner-sharing $[Pb_2I_7]^{\infty}$bilayers and MA^+ cations, which pile up along the *c*-axis. Meanwhile, GA^+ and interlayer MA^+ organic cations are ordered packing between the perovskite layers and linked to the infinite bilayered perovskite *via* N–H···I hydrogen bonds. Especially, due to the small ionic radius of MA (217 pm) and GA (278 pm), the distance between $[Pb_2I_7]^{\infty}$ inorganic layers is as short as 3.125 4 Å [39]. It is noted that such short interlayer distance has a significant impact on their optoelectronic properties, altering their bandgap and dielectric confinement in 2D hybrid perovskites.

As depicted in the ultraviolet-visible absorption spectrum in Fig. 3a, the absorption edge at 680 nm indicates that $GAMA_2Pb_2I_7$ could absorb wide-band visible light. Besides, the optical bandgap is determined by the Tauc plot method [40], and the estimated value extracted from the Tauc plot is 1.88 eV (the inset of Fig. 2a). Meanwhile, we evaluate the band structures and electronic properties of $GAMA_2Pb_2I_7$ crystals by using the first-principles density functional theory (DFT). (Fig. 2b). Both the conduction band maximum (CBM) and valence band minimum (VBM) are obviously located at the same *x*-axis point, which confirms that $GAMA_2Pb_2I_7$ belongs to a kind of direct bandgap semiconductor. The calculated bandgap value of 1.84 eV matches well with the experimental value. Furthermore, the partial density of states (PDOS) spectra demonstrate that the unoccupied I *p* orbitals contribute to the VBM, while the Pb *p* orbitals contribute to the CBM (Fig. 2c).

Based on the good material properties, single-crystal $GAMA_2Pb_2I_7$ photodetectors were constructed using Au as electrodes and glass as a substrate, where the planar device configuration is shown in Fig. 3a. The detailed device fabrication processes were displayed in the experimental section. As the photodetector was made by bulk perovskite single crystal, the crystal anisotropy needs to be taken into consideration [41–43]. As shown in Fig. 3b, the XRD pattern of single $GAMA_2Pb_2I_7$ crystal exhibits periodically repeated diffraction peaks corresponding to the (101) plane group, suggesting the good orientation of the $GAMA_2Pb_2I_7$ single crystal used in this work.

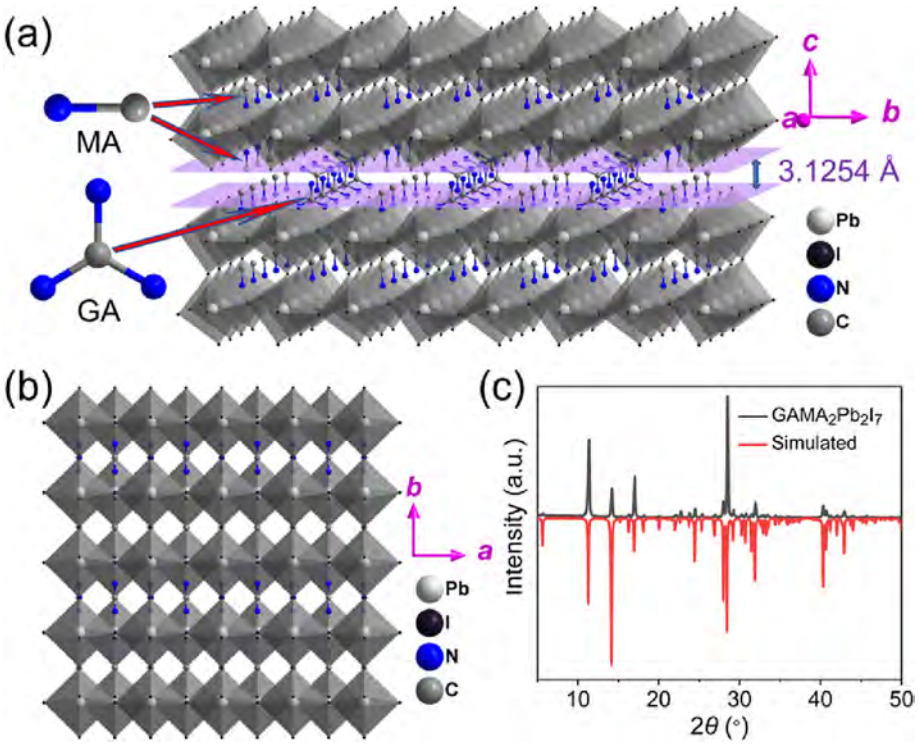

Fig. 1. (a) 2D bilayered crystal structures of $GAMA_2Pb_2I_7$. All hydrogen atoms are omitted. (b) Crystal structure viewed along the *c*-axis direction. (c) Powder XRD pattern and simulated XRD pattern of $GAMA_2Pb_2I_7$.

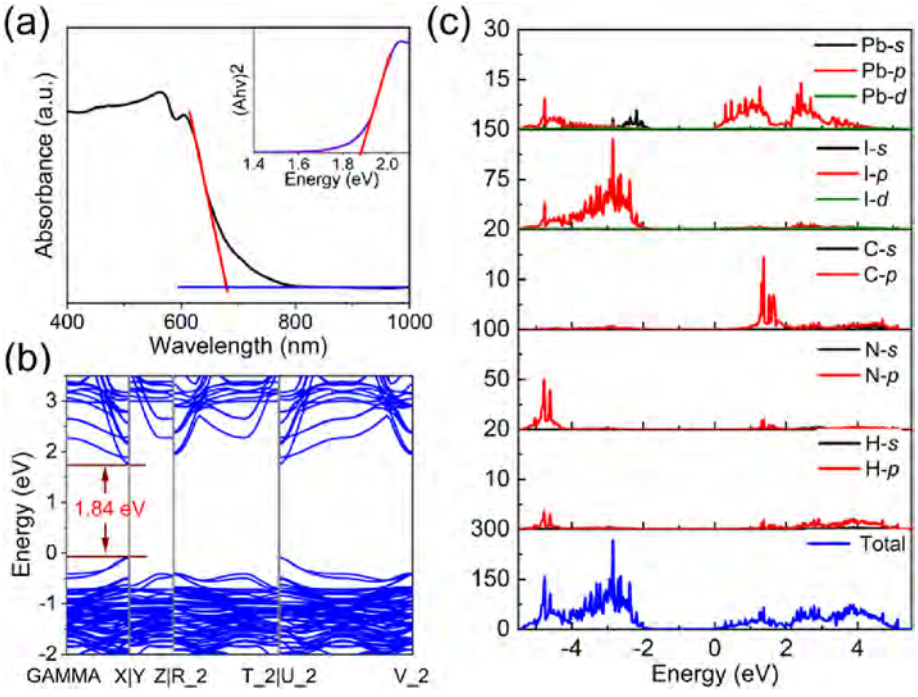

Fig. 2. (a) Absorption spectrum of the $GAMA_2Pb_2I_7$ crystal. Inset: the optical bandgap obtained by the Tauc plot method. (b) DFT calculated band structure and (c) PDOS spectra of $GAMA_2Pb_2I_7$.

First, the spectral response of single-crystal $GAMA_2Pb_2I_7$ was measured with wavelength ranging from 400 nm to 800 nm under an applied voltage of −1.5 V bias (Fig. 3c). The photoresponsivity shows a wide-spectrum response with a cutoff wavelength close to 700 nm, which is consistent with the absorption spectra presented in Fig. 2a. After that, three different incident light wavelengths of 405, 532, and 635 nm were used to characterize the photodetection performance of the $GAMA_2Pb_2I_7$ photodetector. The current–voltage (*I*–*V*) curves in the dark and under different illumination light intensities were recorded with a bias voltage

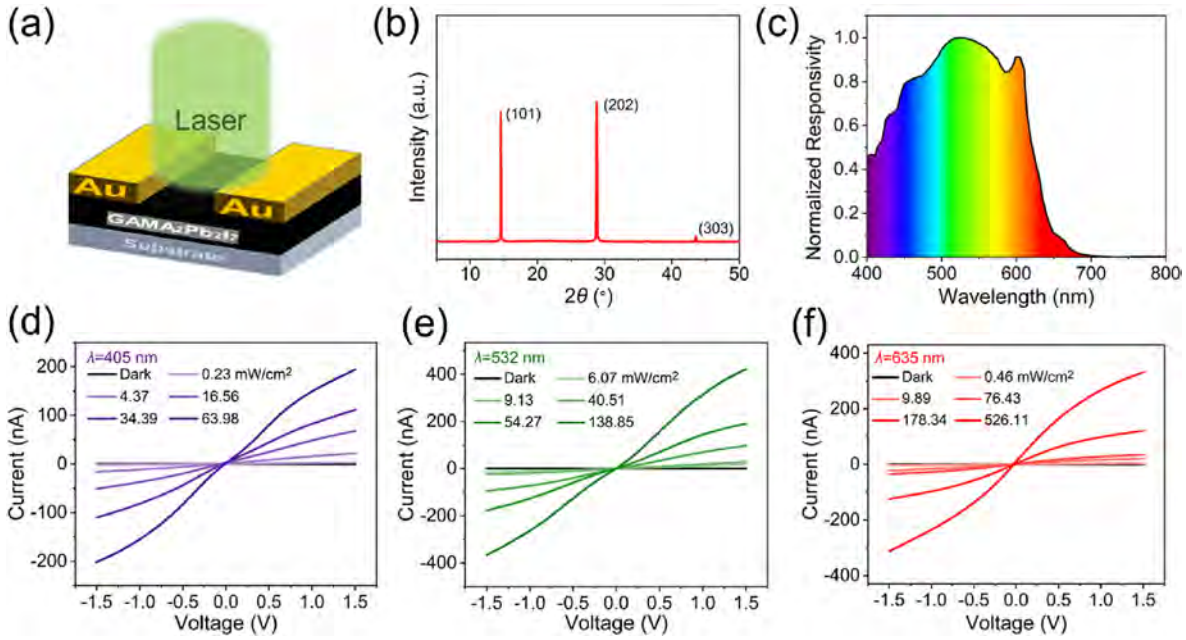

Fig. 3. (a) Schematic diagram of the $GAMA_2Pb_2I_7$ photodetector architecture. (b) XRD pattern of the bulk single crystal of $GAMA_2Pb_2I_7$. (c) Normalized responsivity of the corresponding $GAMA_2Pb_2I_7$ photodetector under the 400-800 nm illumination light. (d, e, f) *I*–*V* curves of dark current and photocurrent under different incident power at −1.5 V (λ = 405, 532, and 635 nm).

of −1.5 V (Fig. 3d-f). The current increased dramatically when the device was illuminated by increasing light intensity. This phenomenon could be attributed to the stronger illumination, which will generate more photogenerated carriers and flow through the channel, causing higher photocurrent in the circuit.

At the same time, the *I*–*T* curves of the $GAMA_2Pb_2I_7$ PDs were also recorded under different illumination of 405 nm, 532 nm, and 635 nm laser at −1.5 V (Fig. 4a, d, and 4g). The measured current shows reproducible on-off switching behaviors under different incident wavelengths and different light illumination powers. The time-resolved *I*–*T* curves of PDs were measured by a homemade high-speed photoresponse measurement circuit, by which the rise and decay times could be estimated from the precise photoresponse signals. The rise time is defined from 10% to 90%, and the decay time is estimated from 90% to 10% of the output signal maximum. As a result, both the rise and decay times are approximately 400 μs in this work, though with different incident light wavelengths, suggesting the fast response of the device (Fig. S4). To understand the photoresponse behaviors, the incident light power versus photocurrent I_{ph} ($I_{ph} = I_{on} - I_{dark}$) is compiled under the illumination of different wavelength light (Fig. 4b, e, 4h), in which the relationship can be fitted by formula 1 [3].

$$I_{ph} = AP^x \tag{1}$$

where *P* represents the photocurrent, while *x* and *A* refer to the fitting exponent and the scaling constant, respectively. Through fitting, the I_{ph} shows a power dependence of 0.86, 0.81, and 0.70 under 405, 532, and 635 nm incident light. Such sublinear correlation between the I_{ph} and the incident light intensity can be attributed to the intricate mechanisms involving exciton generation, trapping, and recombination, which are commonly witnessed in semiconducting materials [44,45].

Besides, to further evaluate the photodetection performance of the $GAMA_2Pb_2I_7$ photodetector, the responsivity (*R*), detectivity (*D**), and EQE were obtained by the following formulas [3,4]:

$$R = \frac{I_{ph}}{Ps} \tag{2}$$

$$D^* = R\sqrt{\frac{S}{2qI_{dark}}} \tag{3}$$

$$EQE = \frac{hcR}{q\lambda} \tag{4}$$

where *S* is the active area of the photodetector, *q* is the absolute value of electron charge (1.6×10^{-19} C), I_{dark} represents the dark current, *h* represents the Planck's constant, *c* refers to the velocity of light, and λ represents the incident wavelength. The light intensity-dependent *R* of the device under illumination with different light intensities were measured, as depicted in Fig. 4b, 4e, and 4h. The high photoresponsivity of 1.56, 2.54, and 2.60 A/W could be achieved for the $GAMA_2Pb_2I_7$ photodetector under 405, 532, and 635 nm incident light under 9.82 nW, respectively, which is larger than those of most reported 2D RP and DJ hybrid perovskite single-crystal photodetectors (Table S1). Furthermore, the *D** and EQE under different light intensities were calculated and shown in Fig. 4c, 4f, and 4i. The largest *D** for the photodetectors under 405 nm, 532 nm, and 635 nm incident light is 1.86×10^{12}, 3.04×10^{12}, and 3.11×10^{12} Jones and the corresponding EQE values are up to 477%, 592% and, 508%, respectively. Moreover, the stability of organic-inorganic hybrid perovskites is essential for practical applications. Fig. S5 shows the *I*–*T* curve of the $GAMA_2Pb_2I_7$ photodetector under 532 nm laser illumination in the ambient temperature (relative humidity is about 68%). The photocurrent maintained 85.5% of the initial performance after 1 000 s operating durations. The thermogravimetric analysis curve also shows high thermal stability up to 260 °C (Fig. S6). These results highlight the operation and thermal stability of the $GAMA_2Pb_2I_7$ crystals, which is beneficial to further practical utilizations.

Based on the outstanding photosensitivity in the visible light region, the $GAMA_2Pb_2I_7$ photodetector holds excellent potential for

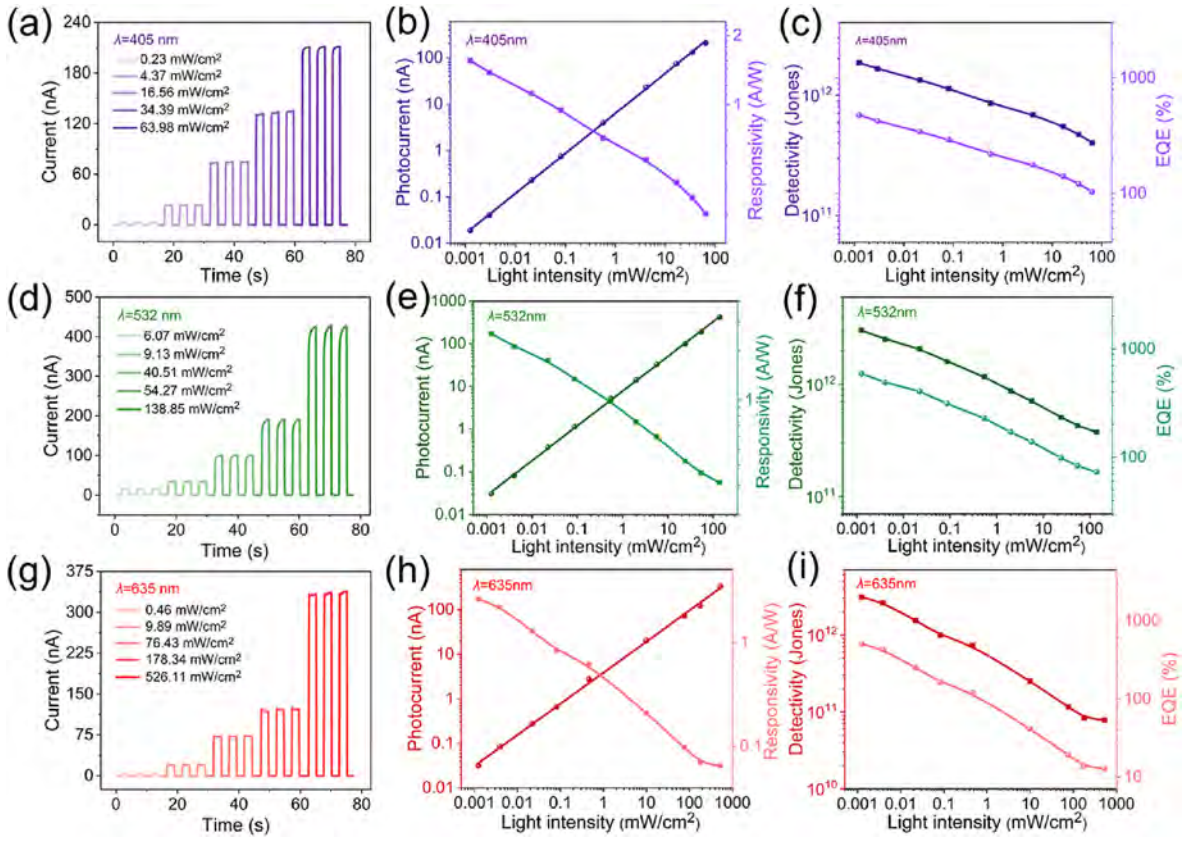

Fig. 4. Performance of the $GAMA_2Pb_2I_7$ photodetector in the visible light spectrum. (a, b, c) The *I–T* curves, I_{ph}, *R*, *D*, and EQE under illumination wavelengths of 405 nm. (d, e, f) The *I-T* curves, I_{ph}, *R*, *D*, and EQE under illumination wavelengths of 532 nm. (g, h, i) The *I–T* curves, I_{ph}, *R*, *D*, and EQE under illumination wavelengths of 635 nm.

imaging applications. Herein, a high-resolution imaging system is built based on the $GAMA_2Pb_2I_7$ photodetector. As shown in Fig. 5a, a laser with a wavelength of 532 nm was used to illuminate the imaging object (a hollow dolphin pattern), which can move sequentially along the *X* and *Y* directions. The $GAMA_2Pb_2I_7$ imaging sensor connected with a semiconductor analyzer was used to record the spatially resolved photocurrent. As a result, a high-resolution dolphin image could be extracted from the recorded photocurrent signal (Fig. 5b), showing the imaging system's good stability and light sensitivity. This work verifies the promising applications in the imaging system based on the 2D bilayered hybrid perovskite with the ACI phase.

4. Conclusion

In this work, an unexplored 2D bilayered hybrid perovskite $GAMA_2Pb_2I_7$ single crystals with the ACI phase was synthesized by a facile solution process. The photodetector with an Au/$GAMA_2Pb_2I_7$/Au device structure was also successfully constructed, showing high photoresponsivity of 1.56, 2.54, and 2.60 A/W for 405, 532, and 635 nm visible light under 9.82 nW, respectively, together with high detectivity values of 1.86×10^{12}, 3.04×10^{12}, and 3.11×10^{12} Jones. Meanwhile, a high-resolution image sensor has been demonstrated under a 532 nm laser to show the excellent photosensitivity and imaging capability. This work shows the great

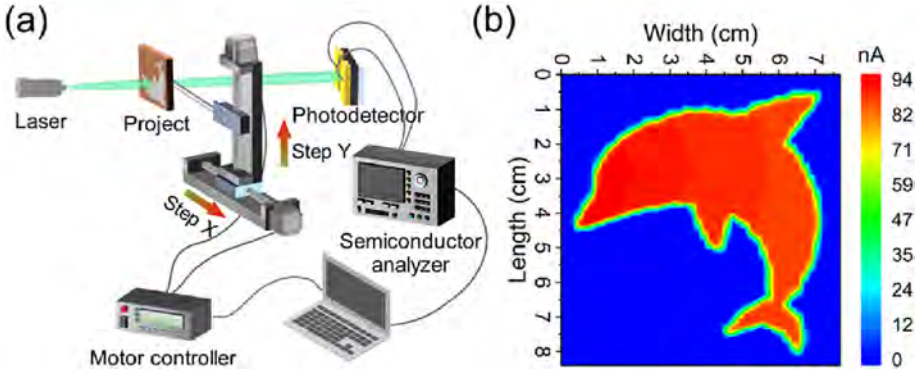

Fig. 5. (a) Schematic diagram of the imaging system based on the $GAMA_2Pb_2I_7$ photodetector. (b) Corresponding imaging results from the fabricated $GAMA_2Pb_2I_7$ image sensor under a 532 nm laser.

potential of 2D hybrid perovskites with the ACI phase for high-performance visible photodetection and imaging applications.

Declaration of competing interest

The authors declare that they have no known competing financial interests or personal relationships that could have appeared to influence the work reported in this paper.

Acknowledgments

This research was financially supported by a fellowship award from the Research Grants Council of the Hong Kong Special Administrative Region, China (CityU RFS2021-1S04).

Appendix A. Supplementary data

Supplementary data to this article can be found online at https://doi.org/10.1016/j.jmat.2023.05.003.

References

[1] Saran R, Curry RJ. Lead sulphide nanocrystal photodetector technologies. Nat Photonics 2016;10:81–92.
[2] Wang F, Zou XM, Xu MJ, Wang H, Wang HL, Guo HJ, Guo JX, Wang P, Peng M, Wang Z, Wang Y, Miao JS, Chen FS, Wang JL, Chen XS, Pan AL, Shan CX, Liao L, W.D H. Recent progress on electrical and optical manipulations of perovskite photodetectors. Adv Sci 2021;8:2100569.
[3] Meng Y, Lan CY, Li FZ, Yip SP, Wei RJ, Kang XL, Bu XM, Dong RT, Zhang H, Ho JC. Direct vapor-liquid-solid synthesis of all inorganic perovskite nanowires for high performance electronics and optoelectronics. ACS Nano 2019;13:6060–70.
[4] Leung SF, Ho KT, Kung PK, Hsiao VKS, Alshareef HN, Wang ZL, He JH. A self-powered and flexible organometallic halide perovskite photodetector with very high detectivity. Adv Mater 2018;30:1704611.
[5] Chen YH, Su LX, Jiang MM. Switch type PANI/ZnO core-shell microwire heterojunction for UV photodetection. J Mater Sci Technol 2022;105:259–65.
[6] Fang Xiaosheng, Huang F, Jia FX, Cai CY, Xu ZH, Wu CJ, Ma Y, Fei GT, Wang M. High-and reproducible performance graphene/II-VI semiconductor film hybrid photo-detectors. Sci Rep 2016;6:28943.
[7] Michel J, Liu JF, Kimerling LC. High-performance Ge-on-Si photodetectors. Nat Photonics 2010;4:527–34.
[8] Huang ZH, Carey JE, Liu MG. Microstructured silicon photodetector. Appl Phys Lett 2006;89:033506.
[9] Xia FN, Mueller T, Lin YM, Garcia AV, Avouris P. Ultrafast graphene photodetector. Nat Nanotechnol 2009;4:839–43.
[10] Wang J, Xing Y, Wan F, Fu C, Xu CH, Liang FX, Luo LB. Progress in ultraviolet photodetectors based on II-VI group compound semiconductors. J Mater Chem C 2022;10:12929–46.
[11] Chen CH, Chang SJ, Chang SP, Li MJ, Chen IC, Hsueh TJ, Hsu CL. Novel fabrication of UV photodetector based on ZnO nanowire/p-GaN heterojunction. Chem Phys Lett 2009;476:69–72.
[12] Wu J, Shao DL, Dorogan VG, Li AZ, Li SB, DeCuir EA, Manasreh JMO, Wang ZM, Mazur YI, Salamo GJ. Intersublevel infrared photodetector with strain-free GaAs quantum dot pairs grown by high-temperature droplet epitaxy. Nano Lett 2010;10:1512–6.
[13] Yamada T, Yamada Y, Kanemitsu Y. Photon recycling in perovskite $CH_3NH_3PbX_3$ (X = I, Br, Cl) bulk single crystals and polycrystalline films. J Lumin 2020;220:116987.
[14] Zhang F, Zhong HZ, Chen C, Wu XG, Hu XM, Huang HL, Han JB, Zou BS, Dong YP. Brightly luminescent and color tunable colloidal $CH_3NH_3PbX_3$ (X = Br, I, Cl) quantum dots: potential alternatives for display technology. ACS Nano 2015;9:4533–42.
[15] Meloni S, Moehl T, Tress W, Franckevičius M, Saliba M, Lee YH, Gao P, Nazeeruddin MK, Zakeeruddin SM, Rothlisberger U, Graetzel M. Ionic polarization-induced current-voltage hysteresis in $CH_3NH_3PbX_3$ perovskite solar cells. Nat Commun 2015;7:10334.
[16] Le N, Truong NTN, Le T, Pallavolu MR, Jeon HJ, Park C. Morphological improvement of $CH_3NH_3PbI_3$ films using blended solvents for perovskite solar cells. Kor J Chem Eng 2021;38:187–94.
[17] Pedro VG, Juarez-Perez EJ, Arsyad WS, Barea EM, Fabregat-Santiago F, Mora-Sero I. J. Bisquert. General working principles of $CH_3NH_3PbX_3$ perovskite solar cells. Nano Lett 2014;14:888–93.
[18] Hou Y, Aydin E, Bastiani MD, Xiao CX, Isikgor FH, Xue DJ, Chen B, Chen H, Bahrami B, Chowdhury AH, Johnston A, Baek SW, Huang ZR, Wei MY, Dong YT, Troughton J, Jalmood RW, Mirabelli AJ, Allen TG, Kerschaver EV, Saidaminov MI, Baran D, Qiao QQ, Zhu K, Wolf SD, Sargent EH. Efficient tandem solar cells with solution-processed perovskite on textured crystalline silicon. Science 2020;367:1135–40.
[19] Wong AB, Lai ML, Eaton SW, Yu Y, Lin E, Dou LT, Fu A, Yang PD. Growth and anion exchange conversion of $CH_3NH_3PbX_3$ nanorod arrays for light-emitting diodes. Nano Lett 2015;15:5519–24.
[20] Asuoa IM, Gedamua D, Kaa I, Gerleina LF, Fortiera FX, Pignoletb A, Cloutiera SG, Nechache R. High-performance pseudo-halide perovskite nanowire networks for stable and fast-response photodetector. Nano Energy 2018;51:324–32.
[21] Tian W, Zhou HP, Li L. Hybrid organic-inorganic perovskite photodetectors. Small 2017;13:1702107.
[22] Ciccioli A, Latini A. Thermodynamics and the intrinsic stability of lead halide perovskites $CH_3NH_3PbX_3$. J Phys Chem Lett 2018;9:3756–65.
[23] Park BW, Seok SI. Intrinsic instability of inorganic-organic hybrid halide perovskite materials. Adv Mater 2019;31:1805337.
[24] Wang K, Wu CC, Yang D, Jiang YY, Priya S. Quasi-two-dimensional halide perovskite single crystal photodetector. ACS Nano 2018;12:4919–29.
[25] Li LN, Sun ZH, Wang Pe, Hu WD, Wang SS, Ji CM, Hong MC, Luo Junhua. Tailored engineering of an unusual $(C_4H_9NH_3)_2(CH_3NH_3)_2Pb_3Br_{10}$ two-dimensional multilayered perovskite ferroelectric for a high performance photodetector. Angew Chem 2017;129:12318–22.
[26] Vasileiadou ES, Wang B, Spanopoulos I, Hadar I, Navrotsky A, Kanatzidis MG. Insight on the stability of thick layers in 2D ruddlesden-popper and dion-jacobson lead iodide perovskites. J Am Chem Soc 2021;143:2523–36.
[27] Lan CY, Zhou ZY, Wei RJ, Ho JC. Two-dimensional perovskite materials: from synthesis to energy-related applications. Mater Today Energy 2019;11:61–82.
[28] Zhou JC, Chu YL. J. Huang. Photodetectors based on two-dimensional layer-structured hybrid lead iodide perovskite semiconductors. ACS Appl Mater Interfaces 2016;8:25660–6.
[29] Tian XX, Zhang YZ, Zheng RK, Wei D, Liu JQ. Two-dimensional organic-inorganic hybrid Ruddlesden-popper perovskite materials: reparation, enhanced stability, and applications in photodetection. Sustain Energy Fuels 2020;4:2087–113.
[30] Tan ZJ, Wu Y, Hong H, Yin JB, Zhang JC, Lin L, Wang MZ, Sun X, Sun LZ, Huang YC, Liu KH, Liu ZF, Peng HL. Two-dimensional $(C_4H_9NH_3)_2PbBr_4$ Perovskite crystals for high performance photodetector. J Am Chem Soc 2016;138:16612–5.
[31] Zhang Yh, Saidaminov MI, Dursun I, Yang HZ, Murali B, Alarousu E, Yengel E, Alshankiti BA, Bakr OM, Mohammed OF. Zero-dimensional Cs_4PbBr_6 perovskite nanocrystals. J Phys Chem Lett 2017;8:961–5.
[32] Zhang BB, Liu X, Xiao B, Hafsia AB, Gao K, Xu YD, Zhou J, Chen YB. High-performance X-ray detection based on one-dimensional inorganic halide perovskite $CsPbI_3$. J Phys Chem Lett 2020;11:432–7.
[33] Wang HP, Li Sy, Liu XY, Shi ZF, Fang XS, He JH. Low-dimensional metal halide perovskite photodetectors. Adv Mater 2021;33:2003309.
[34] Luo T, Zhang YL, Xu Z, Niu TQ, Wen JL, Lu J, Jin SY, Liu SZ (Frank), Zhao K. Compositional control in 2D perovskites with alternating cations in the interlayer space for photovoltaics with efficiency over 18. Adv Mater 2019;31:1903848.
[35] Ghosh S, Pradhan B, Zhang YY, Rana D, Naumenko D, Amenitsch H, Hofkens J, Materny A. Investigation of many-body exciton recombination and optical anisotropy in two-dimensional perovskites having different layers with alternating cations in the interlayer space. J Phys Chem C 2021;125:7799–807.
[36] Soe CMM, Stoumpos CC, Kepenekian M, Traore B, Tsai H, Nie WY, Wang BH, Katan C, Seshadri R, Mohite AD, Even J, Marks TJ, Kanatzidis MG. New type of 2D perovskites with alternating cations in the interlayer space, $(C(NH_2)_3)(CH_3NH_3)nPbnI_{3n+1}$: structure, properties, and photovoltaic performance. J Am Chem Soc 2017;139:16297–309.
[37] Yang J, Yang TH, Liu DL, Zhang YL, Luo T, Lu J, Fang JJ, Wen JL, Deng Z, Liu SZ (Frank), Chen LH, Zhao K. Stable 2D alternating cation perovskite solar cells with power conversion efficiency >19% via solvent engineering. Sol. RRL 2021;5:2100286.
[38] Zhang YY, Keshavarz M, Debroye E, Fron E, González MCR, Naumenko D, Amenitsch H, Vondel JVD, Feyter SD, Heremans P, Roeffaers MBJ, Qiu WM, Pradhan B, Hofkens J. Two-dimensional perovskites with alternating cations in the interlayer space for stable light-emitting diodes. Nanophotonics 2021;10:2145–56.
[39] Kieslich G, Sun SJ, Cheetham AK. An extended tolerance factor approach for organic-inorganic perovskites. Chem Sci 2015;6:3430–3.
[40] Tauc J, Grigorov R, Vancu A. Optical properties and electronic structure of amorphous germanium. Phys Status Solidi B 1966;15:627–37.
[41] Zhou YX, Li JZ, Fang C, Ma JQ, Li L, Li DH. Exciton-phonon interaction-induced large in-plane optical anisotropy in two-dimensional all-inorganic perovskite crystals. J Phys Chem Lett 2021;12:3387–92.
[42] Li JZ, Ma JQ, Cheng X, Liu ZY, Chen YY, Li DH. Anisotropy of excitons in two-dimensional perovskite crystals. ACS Nano 2020;14:2156–61.
[43] Niu XY, Liang LH, Zhang XY, Wang ZY, Zhu TT, Wu JB, Guan QW, Hua LN, Luo JH. Centimeter-sized single crystals of 2D hybrid perovskites toward ultraviolet photodetection with anisotropic photo-response. Mater Chem Front 2022;6:3598–604.
[44] Soci C, Zhang A, Xiang B, Dayeh SA, Aplin DPR, Park J, Bao XY, Lo YH, Wang D. ZnO nanowire UV photodetectors with high internal gain. Nano Lett 2007;7:1003–9.
[45] Lopez-Sanchez O, Lembke D, Kayci M, Radenovic A, Kis A. Ultrasensitive photodetectors based on monolayer MoS_2. Nat Nanotechnol 2013;8:497–501.

Yezhan Li is currently a Ph.D. candidate in the Department of Materials Science and Engineering at the City University of Hong Kong. He received his master's degree in the School of Chemical and Biological Engineering from Guilin University of Technology. His current research mainly explores organic-inorganic hybrid perovskites and their photoluminescence, ferroelectric, and optoelectronic semiconductor properties.

Johnny C. Ho is a Professor of Materials Science and Engineering at the City University of Hong Kong. He received his BS degree in Chemical Engineering and his MS and Ph.D. degrees in Materials Science and Engineering from the University of California, Berkeley, in 2002, 2005, and 2009, respectively. From 2009 to 2010, he was a postdoctoral research fellow in the Nanoscale Synthesis and Characterization Group at Lawrence Livermore National Laboratory. His research interests focus on synthesis, characterization, integration, and device applications of nanoscale materials for various technological applications, including nanoelectronics, sensors, and energy harvesting.